Sound Diffraction Modeling of Rotorcraft Noise Around Terrain

James H. Stephenson *US Army Aviation Development Directorate* *Hampton, VA*

Ben W. Sim *Moffett Field, CA*

Subhashini Chitta *Wave CPC, Inc* *Tullahoma, TN*

John Steinhoff

ABSTRACT

A new computational technique, Wave Confinement (WC), is extended here to account for sound diffraction around arbitrary terrain. While diffraction around elementary scattering objects, such as a knife edge, single slit, disc, sphere, etc. has been studied for several decades, realistic environments still pose significant problems. This new technique is first validated against Sommerfeld's classical problem of diffraction due to a knife edge. This is followed by comparisons with diffraction over three-dimensional smooth obstacles, such as a disc and Gaussian hill. Finally, comparisons with flight test acoustics data measured behind a hill are also shown. Comparison between experiment and Wave Confinement prediction demonstrates that a Poisson spot occurred behind the isolated hill, resulting in significantly increased sound intensity near the center of the shadowed region.

INTRODUCTION

Helicopters are widely used in many applications such as commercial and private transportation, medical emergency, tourism, evacuation and rescue, etc. While many advancements have been made throughout the years, one area that requires further attention is propagation of aerodynamically generated noise over long distances (thousands of wavelengths). The main sources of rotorcraft noise are due to the main rotor and tail rotor; both of which produce lower frequency sounds that are especially capable of propagating over significant distances causing community annoyance complaints across a wide area (Ref. 1).

As a result of helicopter acoustic emissions, several restrictions (Refs. 2, 3) have been imposed to limit the flight operations to specific times and locations, posing an immediate requirement for noise mitigation measures. A critical step toward community noise reduction is to develop a computationally fast noise propagation tool that can account for atmospheric and ground effects, including diffraction. Such a tool will be of great importance in assessing the acoustic impact on populated areas and for finding flight trajectories with optimal noise performance. The focus of this paper is on one important propagation feature, diffraction, which is not currently well modeled for the problem of interest.

Diffraction is a naturally occurring phenomenon that allows waves (including acoustic, electromagnetic, seismic, water waves, etc.) to propagate around objects. Some examples of diffraction include the ability to hear people around corners, optical effects that result in "silver lining" or iridescence of opaque objects, and water wave propagation through breakwaters. Similarly, when a helicopter flies near a hill or other large obstacle such as a building, significant noise levels are observed due to diffraction of sound waves around the obstacle. This is depicted schematically in Figure 1, where the waves from source, S, continue to propagate into the shadow region despite the obstruction.

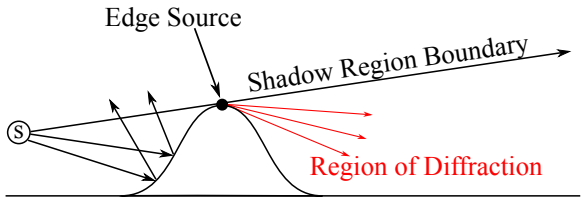

Fig. 1. Schematic depiction of diffraction due to a Gaussian obstruction.

There are several existing aeroacoustic methods that are widely used to solve the above problem but have a broad range of physical and numerical limitations, which restrict their applicability (Refs. 4–6). Some of these methods are based on an inhomogeneous wave equation derived by Lighthill (Ref. 4), where the computational domain is split into a nonlinear source region where a turbulence model is used to evaluate noise sources, and an acoustic region where integral methods such as Kirchhoff (Ref. 6) or Ffowcs-Williams-Hawkings Formulation 1A (F1A) (Ref. 7) are used for propagation. These propagation methods can be used for long distances but are only feasible for uniform media with no scattering topographical features such as buildings or hills.

A closed form equation is usually required in the conventional use of integral methods, to account for wave propagation from each point on an acoustic source surface in an assumed medium to a specified observation point. Thus, for each observation point, the equation has to be integrated over the entire source surface. Reflective and refractive effects require a separate integration over the source surface, which results in a nested integral for each observation point. Account-

Presented at the AHS International 73rd Annual Forum & Technology Display, Fort Worth, Texas, USA, May 9–11, 2017.

ing for each of these effects quickly becomes cumbersome to solve. In such cases, it is more appropriate to use discretization methods to automatically account for the effects due to the environmental factors, including atmospheric conditions (wind, temperature and humidity gradients), terrain (topography, ground impedance) without changing the equations. The price for this generality is that the equations can only be solved over a very limited region since they are restricted to finer grid sizes to reduce numerical dissipation and dispersion errors. Fine grid sizes quickly exceed the memory requirement beyond the capacity of most computers when distances or frequencies increase.

A reasonable alternative to this problem is to use high frequency approximations, such as eikonal or ray tracing. These methods are numerically fast but do not account for sound diffraction effects in an environment with non-flat ground (Ref. 8). To overcome the flat-ground limitation, parabolic methods (Ref. 9) or Geometric Theory of Diffraction (GTD) (Ref. 10) have been coupled with conventional ray tracing techniques. However, it is well known that the parabolic methods tend to become computationally complex and expensive in three dimensions. The latter model, GTD, is computationally cheaper but uses numerical fitting on geometric (2-D) slices through a three dimensional terrain from source to receiver. This method further restricts principle features of the terrain to either: flat, concave, convex, thin screens, or wedges (Ref. 11). This is not physically appropriate in a general sense, and has implications on the accuracy of the final solution.

The persistence of computational difficulty of diffraction modeling, even after decades of research, is a major inhibitor to assess accurate acoustic footprints of rotorcraft. An accurate method to solve diffraction can also help generate new operational guidelines for flight paths and maneuvers that minimize noise levels in populated areas and improve land-use planning. So, a new method that is both computationally fast and accurate is required for propagation of rotor noise over realistic distances and terrain.

It has been well established that grid-based methods are more general in implementation for acoustic propagation over long ranges, but they are currently limited to short ranges (Ref. 12). An improvement that can eliminate this limitation of conventional discrete methods would be a rational approach to solve the problem of interest. A promising improvement is Wave Confinement (WC). WC is a new finite difference formulation of a basic formalism that, to the authors' knowledge, has not been used before in this context. Wave Confinement uses nonlinear solitary waves as basis functions to determine the wave fronts, as treated by Whitham (Ref. 13). Thus, with WC, the evolving acoustic field from a point source can be accurately represented as these propagating wave fronts, which obey the wave equation.

Even though Wave Confinement uses finite differences, it produces stable, asymptotic solutions, unlike conventional discretization methods that eventually decay the solution even with higher order accuracy. This improvement is made possible by adding a nonlinear term to the wave equation, which does not interfere with propagation dynamics, but controls the width of the solution, while conserving the essential integrals of the problem. Wave Confinement has already been proven useful in long range acoustic propagation including effects due to temperature and wind gradients with arbitrary topography (Ref. 14). In this paper, implementation and validation of a new capability that automatically accounts for diffraction is discussed.

METHOD DESCRIPTION

The linearized acoustic wave equation,

$$\partial_t^2 \phi = c^2 \nabla^2 \phi \tag{1}$$

where ϕ is a scalar and c is the speed of sound, is solved using a new grid-based method described below. This involves (a) Wave Confinement for propagation of acoustic wave fronts as asymptotic solutions, (b) Dynamic Surface Extension (DSE) to compute a mapping function between source and far field and (c) Scaling Law (for Diffraction) to apply a correction factor to adjust the amplitude of wave fronts to that of physical waves.

Wave Confinement

Conventional discretizations of Equation 1 are linear and based on polynomial expansions (with coefficients determined by Taylor expansion, perhaps with numerical dispersion minimization). The difficulty with the resulting discretization errors is that they accumulate and continually grow. In these circumstances, higher order methods are often necessary; however, they only delay, rather than eliminate, error accumulation.

By contrast, WC entails a discretization which contains dynamic terms that relax the solution to an equilibrium in the frame of the propagating function. Therefore, error accumulation does not occur; higher order methods become unnecessary since these solutions are stable and can propagate without spreading or dispersing. These solutions are called nonlinear solitary waves, which are well known to arise from a balance between nonlinear and dispersive effects (Ref. 13). The dynamic terms added to the RHS of Equation 1 to produce stable, nondissipative waves are:

$$E = \partial_t \left[\nabla^2 (\mu \phi - \varepsilon \Phi) \right] \tag{2}$$

where Φ is a nonlinear harmonic mean defined as

$$\Phi^n_{i,j,k} = \left[\frac{\sum_{l=-1}^{+1} \sum_{m=-1}^{+1} \sum_{o=-1}^{+1} \left(\phi^n_{i+l,j+m,k+o} \right)^{-1}}{27} \right]^{-1} . \tag{3}$$

Here, ε and μ represent the diffusion coefficient and numerical coefficient, respectively, which stay constant during the entire computation. Equation 1 (with the dynamic terms defined in Equation 2) in discretized form is then written as

$$\phi^{n+1}_{i,j,k} = 2\phi^n_{i,j,k} - \phi^{n-1}_{i,j,k} + \nu^2 (\nabla^2 \phi) + a \delta_n^- [\nabla^2 (\mu \phi - \varepsilon \Phi)] \tag{4}$$

where,

$$\begin{aligned}\nabla^2(\bullet) &= \delta_i^2(\bullet)+\delta_j^2(\bullet)+\delta_k^2(\bullet)\\ \delta_i^2(\bullet)^n &= (\bullet)_{i+1}-2(\bullet)_i+(\bullet)_{i-1}\\ \delta_n^-(\bullet)^n &= (\bullet)^n-(\bullet)^{n-1},\end{aligned}$$

and $v=\frac{c\Delta t}{h}$, $a=\frac{\Delta t^2}{h^2}$, Δt is the time step, and h is the grid cell size. Equation 4 describes all the features of propagation such as reflection, refraction, atmospheric and ground absorption, as well as diffraction. Taylor expansion of this equation can be simplified to an eigenfunction equation with a fixed eigenvalue, whose solutions are nonlinear solitary waves, the details of which are provided in Ref. 15.

This leads to a highly intuitive interpretation where the motion of the physical wave can be represented by evolving wave fronts generated from WC. The main idea that makes this approach feasible is that the position, arrival time (phase), and wavelength of a nonlinear solitary wave are essentially unaffected by discretization error; the profile neither disperses nor diffuses due to discretization effects. Instead, the wave remains concentrated over a small number of grid cells[1], making it possible to consider discrete Eulerian methods as a practical approach for tracking wave fronts over long distances.

This allows the Wave Confinement method to use coarser grids than required by conventional resolution considerations, while accounting for the effects of varying atmospheric and topographic features. Since WC is a grid-based method, it is fairly simple to accommodate varying ground and atmospheric properties. A unique advantage of WC is that it does not need body conforming grids as any topography can be simply immersed in a Cartesian grid. Further, Wave Confinement employs a simple zero contour or level set representation of the surface and can easily accommodate complex shapes with little computational effort.

In addition to tracking position and phase of these nonlinear solitary waves, Wave Confinement also provides an attenuation factor for each wave front[2] arriving at an observer. This allows WC to calculate acoustics amplitude associated with: (a) geometrical distance of travel, (b) terrain acoustics impedance (for ground reflections), (c) atmospheric sound absorption, and (d) sound diffraction. An important note here is that (b), (c) and (d) are frequency-dependent effects. At this initial stage of the computational chain, Wave Confinement derived attenuation factors are strictly valid only for the selected wavelength (see Footnote 1). To accurately account for rotorcraft acoustics that contain a broad range of frequencies, attenuation factors derived from WC are "adjusted" with frequency-dependent scaling laws as explained in ensuing sections.

[1]The wavelength of the nonlinear solitary wave used in current studies typically covers five to seven grid cells.

[2]There may be multiple wave fronts due to reflections/refractions that arrive at a single observer.

Dynamic Surface Extension

If the source is omnidirectional, computation of phase and attenuation factor are enough to construct the acoustic signature at any far field point. However, rotorcraft noise has angular dependence (i.e., nonuniform sound source), which can be captured directly by propagating the waveform on the grid or by using Dynamic Surface Extension (DSE) (Refs. 14, 16). The former is not feasible since grid-based methods dissipate the waveform. The latter, which uses a mapping function that maps each point in $\mathbb{R}^3$ to the source surface to compute the waveform, is not numerically dissipative/dispersive. This involves propagating a set of conserved variables (e.g., initial emission angles) from known points on the source sphere to far field locations in the same way as the scalar, ϕ, shown in the previous section. These conserved variables propagate on the characteristics, or lines that are normal to the evolving wave fronts (see Figure 2), and therefore, stay invariant in that direction. So, at any far field point, (x,y,z), a set of emission angles (q_r,q_s) corresponding to each pass of the wave are computed.

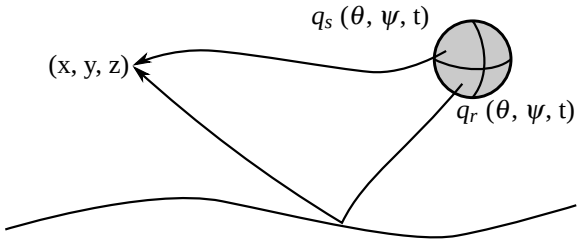

Fig. 2. Dynamic surface extension mapping of source sphere to destination location.

The acoustic signal at any far field point will then be

$$p(\bar{\mathbf{x}},t)=\sum_{i=1,n}R_i(\bar{\mathbf{x}})*p(\psi_i(\bar{\mathbf{x}}),\theta_i(\bar{\mathbf{x}}),t+\tau_i(\bar{\mathbf{x}})) \qquad (5)$$

where $\bar{\mathbf{x}}$ is location in (x,y,z), R is the attenuation factor, i is the index of the arrival, ψ and θ are azimuth and elevation angles respectively, τ is the emission time, and n is the number of arrivals. Dynamic Surface Extension was later renamed by others as "closest point method" (Ref. 17); however, the concept of mapping the surface along propagation paths is identical. With this new approach, details of physical waveforms are not numerically propagated, only locations of the origin where the waveforms are known. This approach has already been validated for long range propagation, including refraction and multiple reflections (Ref. 14). Validation of this method for diffraction will be demonstrated in this paper.

DIFFRACTION

According to Huygens' principle of wave theory (Ref. 18), each point on a wave propagates as a point source. This is expressed as $A=\frac{A_0}{r}e^{-i\omega t}$, where A_0 is the source strength, r is the distance of propagation and ω is the frequency. For example, in Figure 3a, the wave front at $t_2=t_1+dt$ is constructed

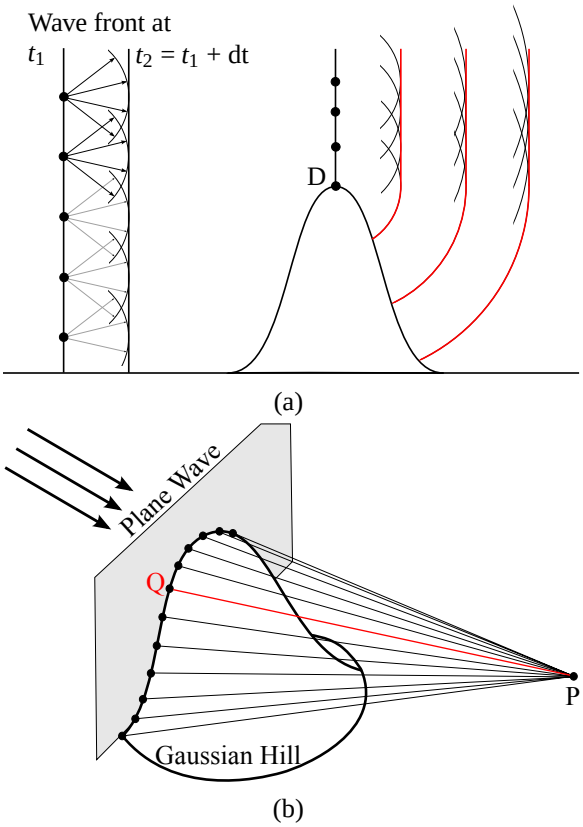

Fig. 3. Description of diffraction using Huygens' Principle for a (a) 2D and (b) 3D case.

by applying the principle of composition to the wavelets generated by each point on the wave front at an earlier time, t. These wavelets cancel each other at oblique angles of incidence in free space. However, when there is an obstruction, only part of the wave travels unimpeded. These unimpeded wavelets interact with the obstacle, essentially acting as new sources. The oblique wave portions no longer cancel each other; instead, they form a secondary wave that propagates into the shadow region. This is defined as a diffracted wave.

The total field associated with a scattering object is the sum of the incident field, reflected field, and diffracted field. High frequency approximations can accurately predict incident and reflected fields (if surface normals are specified with reasonable accuracy). However, diffraction is a frequency dependent problem that cannot be solved with a high frequency assumption. Sommerfeld, Keller, Kirchhoff and other researchers (Refs. 10, 19, 20) have carefully studied this phenomenon and presented solutions for diffraction due to a knife edge, single slit, double slit, disk, sphere, etc. Although these methods work quite well for simple scattering objects, they are not feasible in realistic environments, where obstacles are not well defined and no closed form solutions exist.

Another attempt to solve the diffraction problem was to couple the high frequency approximation to Geometric Theory of Diffraction (Ref. 11). As previously discussed, however, this does not account for realistic spreading. For example, Figure 3b shows a plane wave propagating over a Gaussian hill, each point on the wave front acts as a point source and the information is propagated in *all* directions. The secondary waves in this case are spherical and not confined to a single plane. Therefore, the amplitude at a point (P) is due to the wavelets from all the planes. This also proves that solving the diffraction problem as 2D slices neglects spherical spreading.

To demonstrate this property, wave propagation over a Gaussian hill is computed using both 2D and 3D approximations, shown in Figure 4. For 2D, a cylindrical source, equivalent to a line source in 3D, is propagated separately in each y-slice, using a 2D wave equation. There is no interaction between the slices and the spreading is confined to a specific slice. It is as if the information from only one point (Q) is reaching the far field point (P) in Figure 3b.

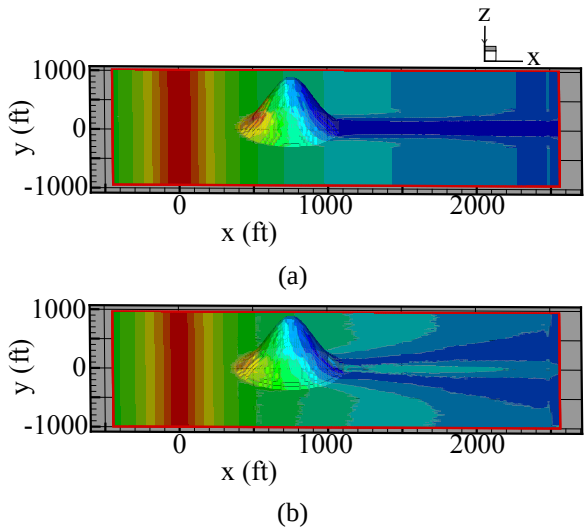

Fig. 4. Diffraction computation (a) solved as 2D slices vs (b) 3D. Red identifies high sound intensity, while blue is low sound intensity.

For the 3D case, a line source is propagated using the three dimensional wave equation. The amplitude at a point, P, takes into account spherical spreading from all points Q, which is in agreement with Huygens' Principle. As can be seen in Figure 4, the amplitude computed with the 2D slice assumption is significantly different from the 3D solution. Note that the amplitude is much stronger behind the object at the center of the shadow region, due to constructive interference of the waves emanating from the edge surface. This is called a Poisson spot, which is not observed in the 2D computation, and has implications to the flight test data.

Knife Edge Diffraction

The proposed method is first validated against the classic diffraction problem of a plane wave propagating over a perfectly reflecting semi-infinite plane as shown in Figure 5. The exact solution of this problem was originally solved by Sommerfeld (Ref. 19) in the frequency domain. A number of other researchers subsequently developed solutions using a variety

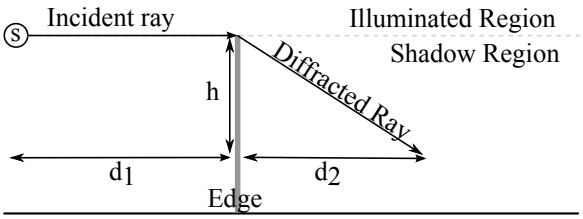

Fig. 5. Schematic of a wave diffracting due to a knife edge.

of methods such as Green's functions, Fourier/Laplace transforms, etc.

Here we will use Wave Confinement to solve this problem, with the following computational setup. The knife edge is considered to be along the y-axis (vertical axis), extending to $y = 1000$ ft, and is positioned at $x = 1000$ ft along the horizontal axis. The computational plane wave is initialized at $x = 0$ ft, which is then propagated from left to right using Equation 4 as a codimension one structure, $\phi = A_0(\operatorname{sech}\alpha(\vec{x}-\vec{x}_0))$. Here, $\vec{x}_0$ is the centroid (position) and α defines the width (or the central wavelength) of the computational wave. α is a function of the confinement parameters, ε and μ. The time evolution of these propagating computational waves is shown in Figure 6, which demonstrates that unlike conventional high frequency approximations that solve ODEs along the ray, the linear wave equation does not discontinuously decrease amplitudes at the shadow boundary.

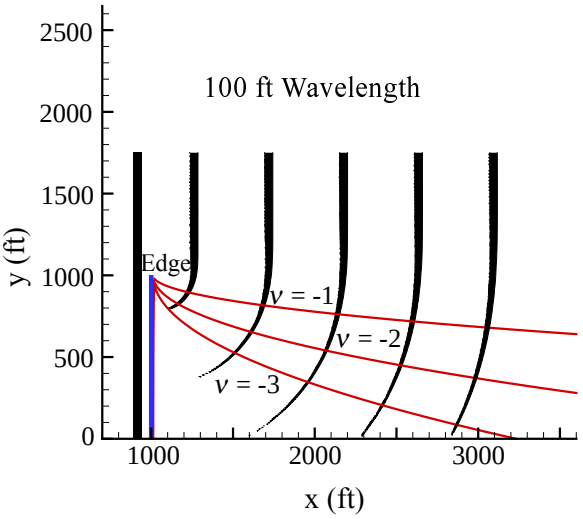

Fig. 6. Time evolution of codimension one surfaces propagating (to the right) over a knife edge using Wave Confinement.

The diffraction loss (L_c) is computed using the relations,

$$L_{c_{i,j,k}} = 20\ \log\left(\frac{A_{i,j,k}}{A_0}\right) \tag{6}$$

and

$$A_{i,j,k} = \int \phi_{i,j,k}\, dt. \tag{7}$$

As mentioned previously, L_c correspond to the wavelength of the computational wave, which is scaled and compared to the approximated analytical diffraction loss (L_a) defined by Ref. 21 as,

$$L_a = \begin{cases} 20\log(0.225/|\nu|), & \nu <= -2.4 \\ 20\log\left[0.4 - \sqrt{\left(0.1184 - (0.38 - 0.1\nu)^2\right)}\right], & -2.4 < \nu <= -1 \\ 20\log(0.5e^{0.95\nu}), & -1 < \nu <= 0 \\ 20\log(0.5 + 0.62\nu), & 0 < \nu <= 1 \\ 0, & \text{otherwise.} \end{cases} \tag{8}$$

Here, ν is a nondimensional variable defined as

$$\nu = h\sqrt{\frac{2}{\lambda_s}\left(\frac{1}{d_1} + \frac{1}{d_2}\right)}, \tag{9}$$

where d_1 is the normal distance between source (S) and the edge, and d_2 is the normal distance between the observation point and the edge, as depicted in Figure 5.

Since the incident wave is assumed to be planar (i.e., $d_1 \to \infty$), ν reduces to $\nu = h\sqrt{\frac{2}{\lambda_s d_2}}$. h is defined as, $h = y - y_0$ where y is the height of the observation point and y_0 is the height of the edge (1000 ft in Figure 6). So, below the edge, $h < 0 \Longrightarrow \nu < 0$. For example, in Figure 6, contour lines corresponding to $\nu = -1, -2, -3$ are shown, all of which are below the edge of the semi-infinite plane.

Both L_c and L_a are independent of wavelength when they are plotted as a function of ν, which means Figure 7 is true for all wavelengths. It can be seen in Figure 7 that the computed diffraction loss (L_c) is in good agreement with the analytically determined diffraction loss (L_a), validating the ability of Wave Confinement to capture diffraction for the knife edge case.

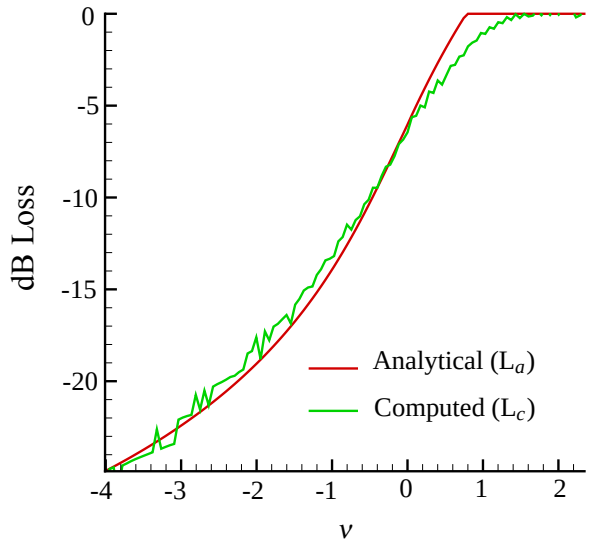

Fig. 7. Diffraction loss plotted as a function of ν, plotted at x = 2000 ft from Figure 6.

Scaling Law

While WC gives an accurate solution, it is not feasible to repeat Equation 4 for each frequency separately. Thus, a scaling law is required. This scaling law is used to correct the amplitude of the computational wave, A_c, for any physical wavelength, λ_p. This is generalized to an arbitrary shape of the obstacle with reasonable accuracy, and is defined as,

$$A_p = A_c \sqrt{\frac{\lambda_p}{\lambda_c}} \tag{10}$$

where A_p is the amplitude of physical wave and λ_c is the wavelength of the computational wave.

Equation 10 can be checked using an analytical solution from the knife edge diffraction case previously described. We assume a computational (or reference) wavelength of 200 ft, and calculate A_p (for all wavelengths) and A_{200} using the equation $A_\bullet = 10^{L_{a\bullet}/20}$, where L_a is defined in Equation 8. Figure 8 shows the ratios, $\lambda_p/200$ and A_p/A_{200}, for different values of h below the edge, as defined in Figure 5. It can be seen from Figure 8 that Equation 10 becomes more accurate further into the shadow region. So, a predetermined table of ratios computed using the equations above can be used in future simulations, with an assumption that the size of the obstacle is greater than the computational wavelength.

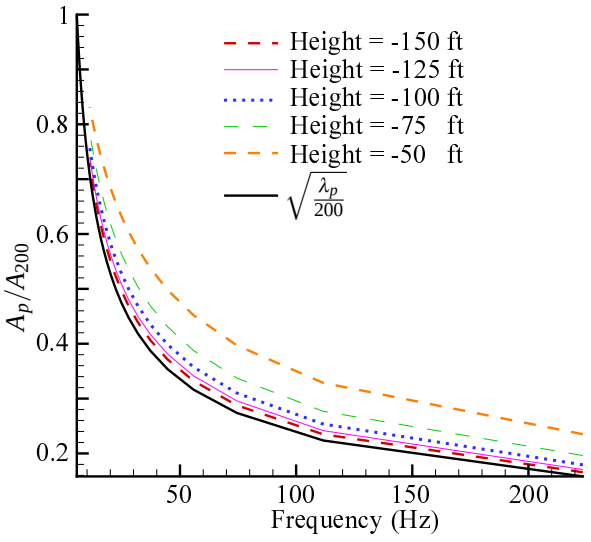

Fig. 8. Scaling factor plotted as a function of frequency. Scaling factor is calculated at various heights beneath a knife edge, for a given 200 ft computational wave.

Propagation over realistic terrain

In realistic environments, there are no flat grounds or knife edges. The scattering surfaces are not aligned to the computational grid, and an accurate immersed boundary condition is required. As mentioned earlier, Wave Confinement uses a level set approximation to specify a boundary. This means

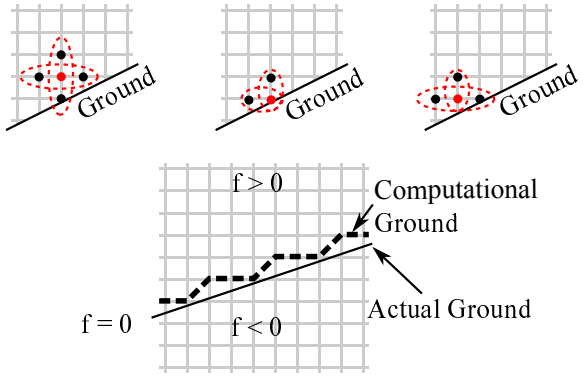

Fig. 9. Stencil used for computation.

that the boundary is represented by a function, f, which on any grid point is $<$, $>$, or $=0$. Since Cartesian grids are used here, the physical boundary does not necessarily fall on grid points, as shown in Figure 9. The practical implementation of this scheme is that the computational waves reflect from the computational ground. This can result in a small error in the phase computation, which is approximately constant everywhere and can be added during the post-processing. For simplicity, it is assumed here that the computational ground is the actual ground. Further, it is assumed that all reflections are specular in nature.

The derivatives at the ground are computed using the stencil shown in Figure 9. At the ground, one or more grid nodes in the stencil are below the boundary, in which case, they are interpolated using the ones above. This does not involve complicated logic since function f automatically defines whether a grid point is above or below ground. Also, Wave Confinement uses low order discretizations. So, there is never more than one grid point in each direction that needs to be interpolated, which makes WC computationally cheaper than existing grid-based methods. Also, despite the initial staircase effect, the reflected wave fronts quickly become smooth due to tangential dissipation (Ref. 14).

To demonstrate the immersed boundary condition, diffraction of a normally incident plane wave due to a circular disk is shown. This is a canonical diffraction problem, the closed form solution of which is not as straightforward as that of semi-infinite half plane (Ref. 22). The diffraction pattern depends on the ratio of perimeter to wavelength, $\frac{2\pi}{\lambda}a$ or ka, where a is the radius of the disk and k is the wavenumber of the plane wave. For $ka >> 1$, the diffraction pattern is calculated using the computational setup shown in Figure 10. The disk is aligned to the $y-z$ plane defined using the boundary function, $f = y^2 + z^2 - a^2 = 0$, with radius (a) of 200 ft. The plane wave is represented by the scalar, ϕ, and has a thickness of 50 ft. As the wave propagates over the disk, each point on the disk acts as an edge source, which constructively interferes to form a bright spot (Poisson spot), shown in Figure 11.

The quantity, $\left(\frac{\int \phi dt}{\phi_0}\right)^2$, which is a representation of Intensity ratio, $\frac{I}{I_0}$ is plotted on a $y-z$ plane behind the disk in

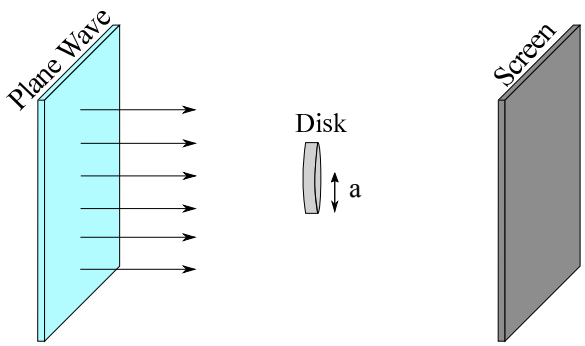

Fig. 10. Computational setup for scattering over disk.

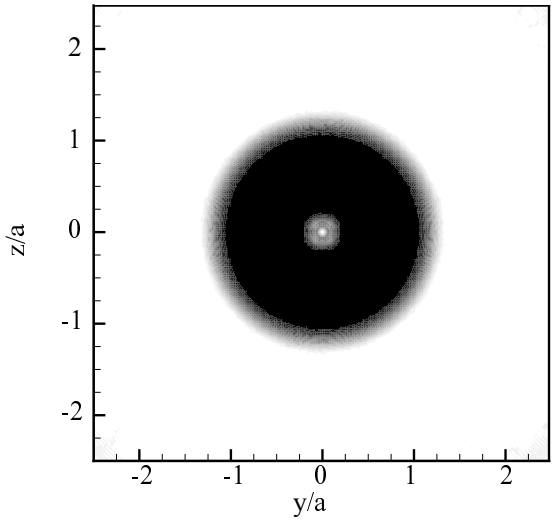

Fig. 11. Plot of intensity on the $y-z$ plane behind a disk.

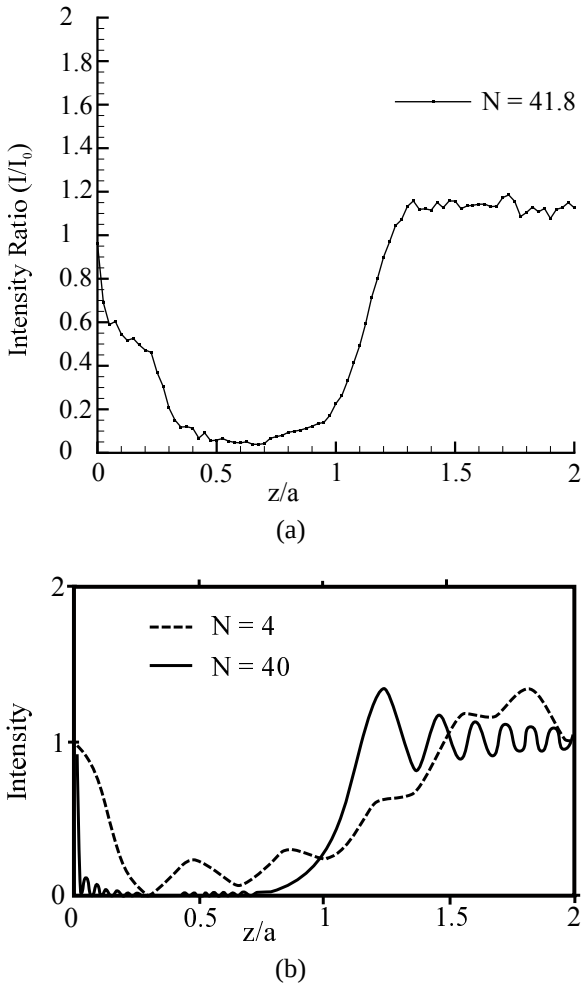

Fig. 12. Intensity ratio from Figure 11, for y = 0 line. Intensity ratio (a) computed using Wave Confinement, compared with an (b) analytical solution. (b) is digitally traced from Ref. 23.

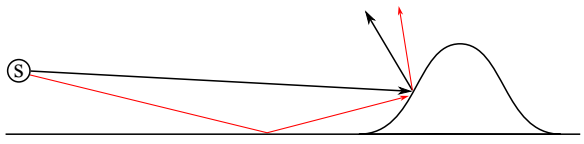

Fig. 13. Multiple reflections depicted using a Gaussian hill.

Figure 11, to show the Poisson spot. The intensity ratio is also plotted as a function of z/a, at y = 0 for $v = \frac{x}{\pi}\frac{\lambda}{a^2}$ (or $N = \frac{1}{v} = 41.8$) in Figure 12. This is compared with an analytical solution from Ref. 23. Note that this method does not need to be used to compute the interference pattern in the illuminated region ($z/a > 1$), since the incident wave has much higher amplitude. The solution for the proposed diffraction model is shown to have a qualitative agreement with the analytical solution for locations $z/a < 1$, with some discrepancies at $z/a < 0.4$.

Ground topography can be more complex than elementary objects like disks and spheres. However, it is still possible to immerse highly complex geometry in a Cartesian grid in a similar manner as described. Further, realistic ground can lead to more than one reflection. An example of multiple reflections from a single point is shown in Figure 13. The ray reflected from one part of the ground (flat ground) can reflect again from another location (Gaussian hill). In such cases, there is a phase difference between both waves which can significantly affect the total signal unless the phase difference is much smaller than the wavelength.

Figure 14a depicts an omnidirectional acoustic wave propagating over an isolated hill. This figure shows a secondary wave front due to multiple reflections, as described in Figure 13. Since Wave Confinement is a grid-based method, these wave fronts need to be separated by at least 5 grid cells to capture the phase difference between them (see Figure 14b). If the grid cell size is increased for the same computation, there are not enough grid points to separate these waves, and they merge as if there is no phase difference, shown in Figure 14c.

The merger of incident and reflected wave is an acceptable approximation for waves on the same order as the computational wave, but is invalid for the problem of interest, where the physical waves are much shorter and phase differences become significant. In other terms, if the amplitudes of these two waves are $|A_1|$ and $|A_2|$, respectively, the intensity is computed as $(|A_1|+|A_2|)^2$. However, a physically accurate calculation would yield $|A_1+A_2|^2$, which is

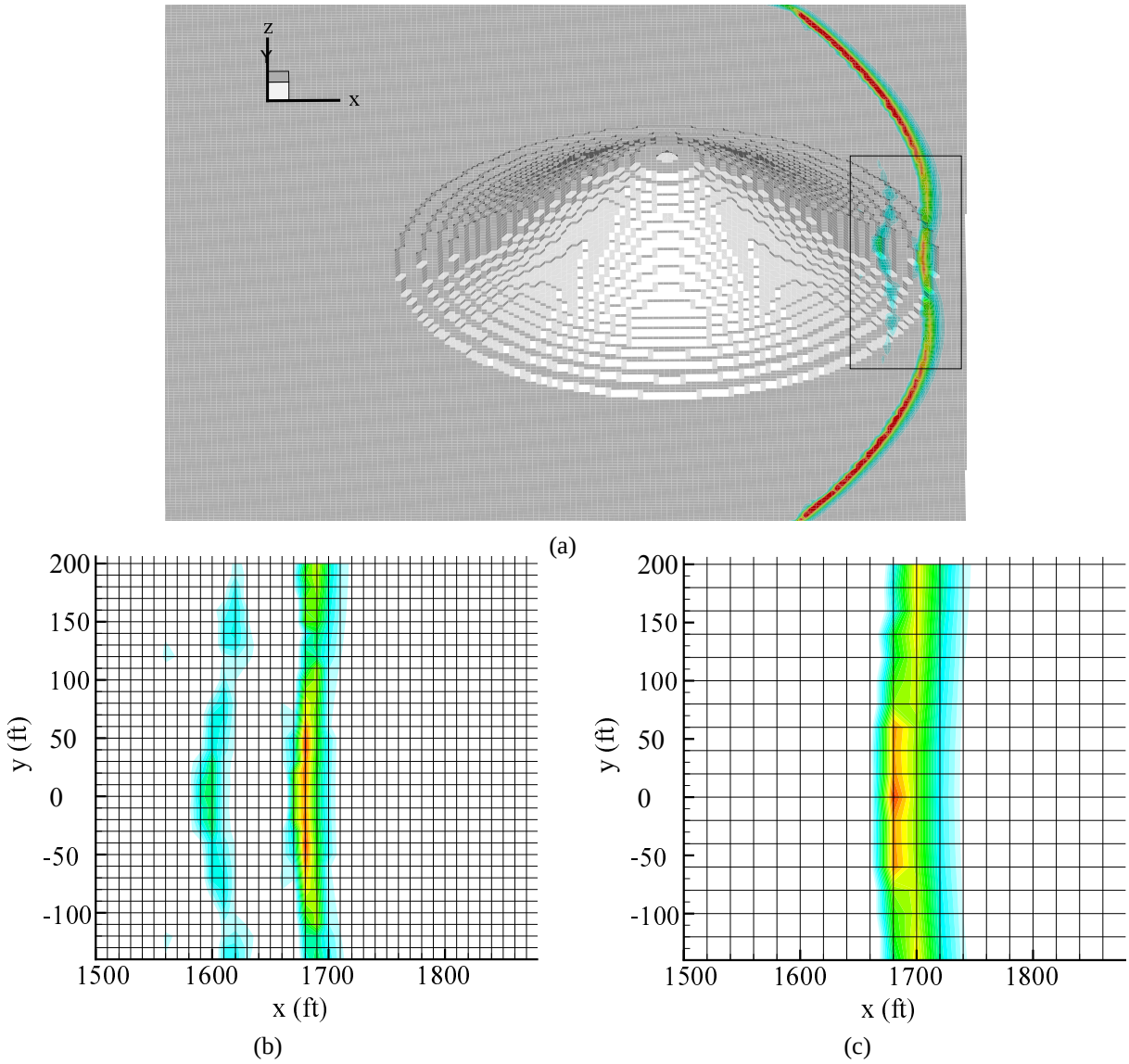

Fig. 14. (a) Time snapshot of computational wave on fine grid. Close-up view of computational waves on a (b) fine and (c) coarse grid. Darker colors (red) indicate higher sound intensity.

$|A_1|^2 + |A_2|^2 + 2|A_1||A_2|cos\delta$, where δ is the phase difference. The current implementation of Wave Confinement results in this limitation, but it will be overcome in the future by solving the reflected wave in a separate array.

FLIGHT TEST COMPARISON

Helicopter acoustic data from an AS350 SD1 vehicle were acquired in Sweetwater, NV in 2014. The flight test data include acoustic measurements from behind an isolated hill. Figure 15 shows the microphone locations with microphones behind the isolated hill identified as microphones 27 thru 29. The full test description can be found in Reference 24, while relevant parameters are provided here. The AS350 SD1 is a 3000 pound civilian aircraft with a main rotor blade passage frequency of 20 Hz, with a tail rotor blade passage frequency of 70 Hz. Acoustic data acquisition for each level flight case started when the vehicle was approximately 4000 ft before the main microphone array (microphones $1-21$), and terminated approximately 4000 ft after the main array.

Pressure time-series data from microphones 27 thru 29 are high-pass filtered using a 5^{th} order Butterworth filter with a cutoff frequency below 10 Hz. This high-pass filtering is required to remove wind noise from the measurement data in order to better identify the faint acoustic signals arriving from the vehicle.

Source Hemisphere

Source hemispheres from steady level flight conditions can be created using the main microphone array. The hemisphere used for this paper has a radius of 100 ft, and comes from a 105 knot level flight condition with very low background wind speeds (less than 1 knot at flight altitude). Pressure

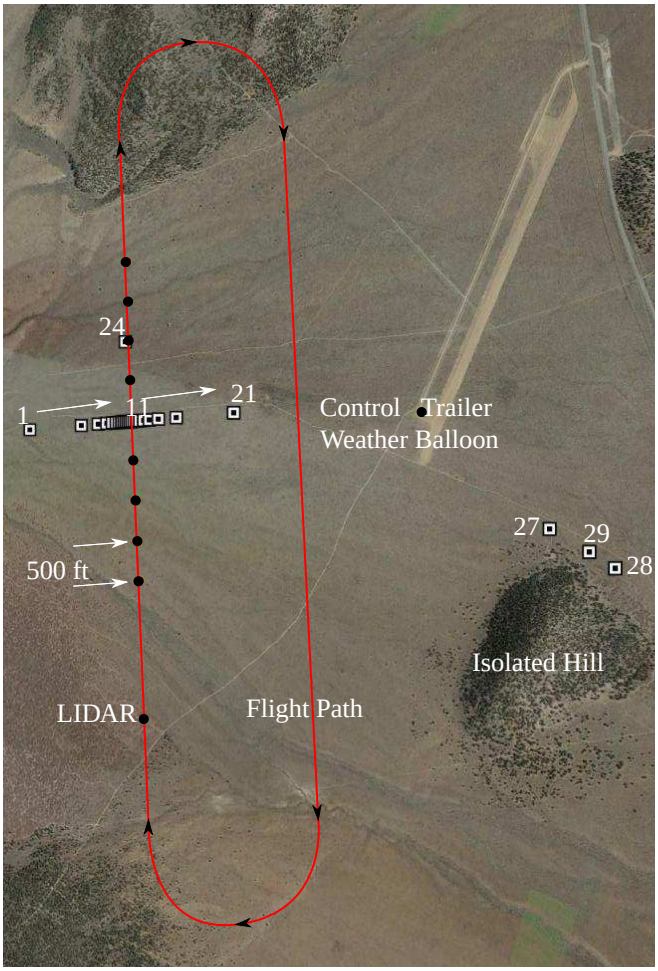

Fig. 15. Equipment locations with notional vehicle flight path and local geography shown.

data are corrected for pressure doubling at the ground, and transformed from time of reception to time of emission, de-Dopplerized, and corrected for spherical spreading (Ref. 25).

Pressure time-series data from microphones 1-21 (sub-sampled to 12 kHz) are stored in half-second increments, with 50% overlap, at the 'average' elevation and azimuth on the vehicle, as experienced during each half second time increment. Figure 16 is a Lambert projection of the overall sound pressure level of the hemisphere for this run. Each dot represents a half second of stored pressure time-series data at every quarter second (50% overlap) throughout the duration of the steady level flight.

The AS350 SD1 main rotor rotates clockwise when viewed from above, so the Lambert projection begins with an azimuth of 0° at the tail, 90° azimuth is on the left side of the vehicle, while 270° is on the right side of the vehicle. Elevation begins in the plane of the rotor (0°) at the edge of the Lambert projection and decreases radially such that directly beneath the rotor (−90°) is represented by the point in the center of the Lambert projection. The pressure time-series hemisphere data are used to propagate signals to microphones 27 thru 29, from a known and measured vehicle location.

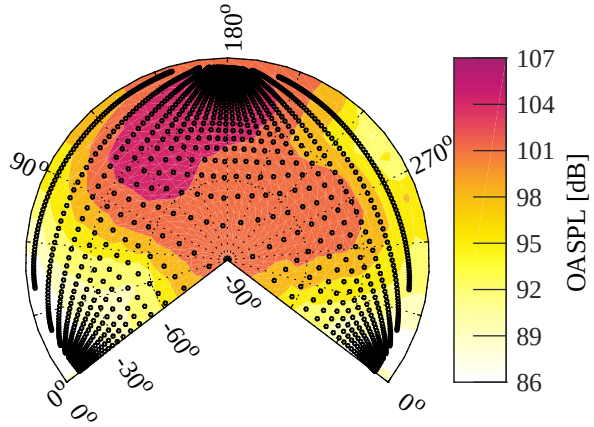

Fig. 16. Lambert projection of the overall sound pressure level [dB], with markers identifying each segment of half-second pressure time-series data.

Far Field Computation

The computational-setup of the flight test for a fixed aircraft position is described below:

First, the size of computational domain (in physical units) centered at microphone 11 is defined as shown in Figure 17. Ground elevation data of ≈ 150 ft resolution for this domain are imported from Google earth. Terrain data were rotated to align with the flight direction and then linearly interpolated on a Cartesian grid (x,y) with nodes located every 20 ft and altitude (z) calculated through linear interpolation from nearest neighbors. Interpolated altitude was grounded using the measured GPS location of microphone 11 and verified against all microphone locations. The ground interpolation scheme was accurate within -2.2 to $+0.9$ feet for the main microphone array and within 8 feet for the diffracted microphones.

For the purposes of this paper, x is defined as the direction of the flight path, with y to the left of the vehicle. The origin is located at the reference microphone location (microphone 11). The terrain data are then immersed in a 20 ft incremented

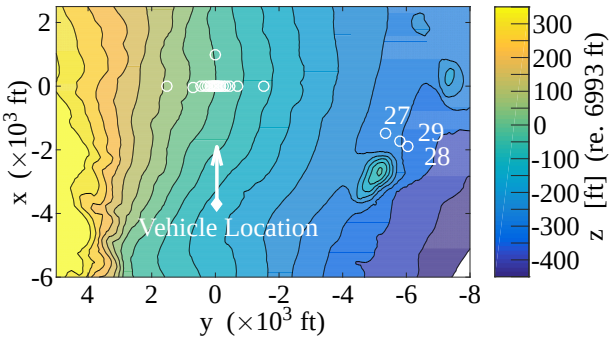

Fig. 17. Computational domain with origin at microphone 11, (reference altitude 6993 ft mean sea level). Contour lines are every 50 ft of elevation.

Cartesian grid (x,y,z) using the boundary function,

$$f = \begin{cases} 0, & z - z_{elevation} <= 0 \\ 1, & \text{otherwise.} \end{cases} \quad (11)$$

The locations of the microphones used for comparison are shown in Table 1. There is an offset between measured locations and computed location because the physical ground does not align with the grid. Second, the source surface, represented by isotropic spherical wave is initialized at a radius of 170 ft, around the aircraft positioned at $(-3701, -48.5, -252.2)$ identified as 'Vehicle Location' in Figure 17.

Table 1. Microphone locations as measured versus nearest computational grid locations.

Mic #	Measured (x, y, z ft)	Computed (x, y, z ft)
10	(2.1, 26.9, 1.6)	(0, 20, 0)
13	(3.3, -60., -3.2)	(0, -60, 0)
17	(-0.3, -235.6, -12.7)	(0, -240, -20)
27	(-1480.2 -5345.6 -280.9)	(-1480 -5340 -280)
28	(-1908.7 -6048.7 -316.8)	(-1900 -6040 -320)
29	(-1732.6 -5780.6 -303.1)	(-1740 -5780 -300)

With the vehicle location, source noise, and terrain defined, Equation 4 can now be solved to compute phase, attenuation factor (which includes the effect due to diffraction), and emission angles. For the purposes of this diffraction investigation, the terrain is assumed to be a hard surface and atmospheric attenuation has been turned off. However, Wave Confinement is capable of accounting for each of these effects (Ref. 14).

The pressure time histories at microphones 10, 13 and 17, which are in line of sight, are extracted using the mapping function and compared to the measured data in Figure 18. Computed and measured data are in excellent agreement, which is to be expected since the source surface is constructed using the recorded data from these microphones. Further, the data were forward propagated using the same atmospheric and ground conditions as that of backward propagation used to form the spheres. This validates that the computational setup and the algorithm are in agreement with the source data for the simple straight ray case.

Pressure signals from the source hemisphere are then propagated to microphones 27-29, behind the isolated hill. Figure 19 shows the computed attenuation factor (for approximately 5 Hz[3]) near these microphones. It was anticipated that sound intensity at microphones 27 and 28 would be higher than at microphone 29, which is confirmed by the measured data as shown in Figure 20. It was anticipated that further behind the hill, the sound intensity would decrease. However, as can be seen from Figure 19, microphone 28 is in a Poisson spot

[3]Wave front is 5-7 grid cells wide, with grid cells spaced every 20 feet. This results in an approximately 4 to 5.5 Hz wave.

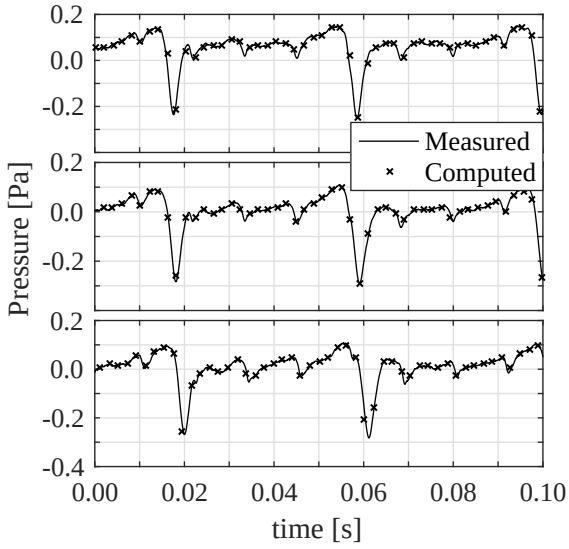

Fig. 18. Comparison of computed versus measured pressure time-series data for microphone (top) 10, (middle) 13, and (bottom) 17. Every 30^{th} time stamp of the computed signal is shown for clarity.

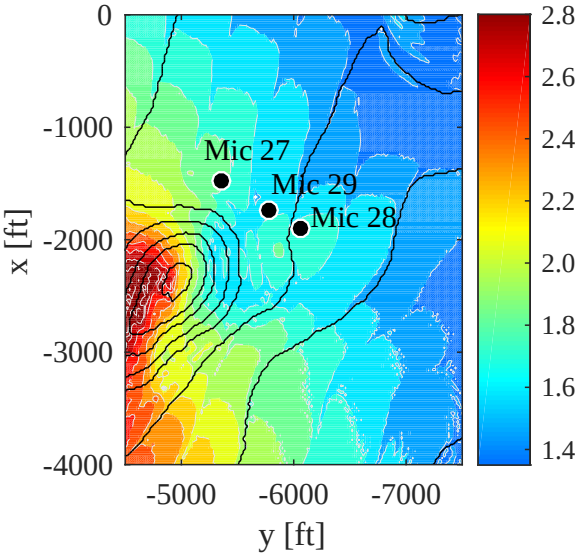

Fig. 19. Computed attenuation factor (x 10^{-4}) for an approximately 5 Hz wave propagating around the isolated hill, with microphones 27 thru 29 identified. Black lines are 50 foot elevation lines from Figure 17.

formed by the hill. This resulted in a higher measured value than that seen by microphone 29, which was more "line of sight". The prediction of this Poisson spot not only helps validate the proposed propagation method, it elucidates the apparent anomaly seen in the measured data, and confirms that 2D methods are not adequate for real life scenarios.

Now, the frequency spectrum at each of the isolated hill microphone locations is calculated using the closest available data point on the source hemisphere. Table 2 shows the difference in azimuth and elevation angles from available source

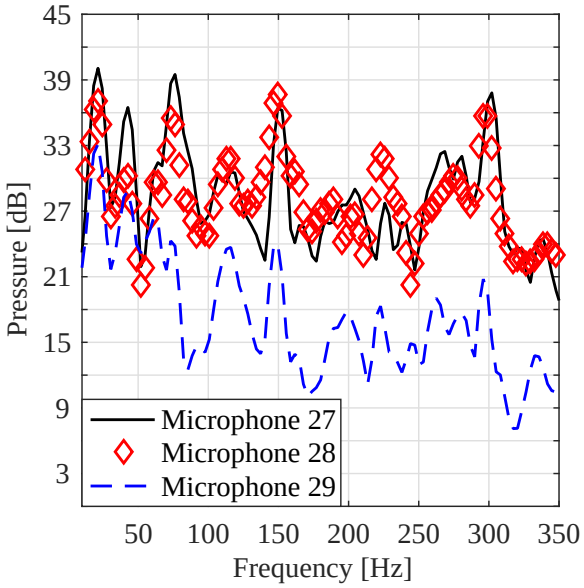

Fig. 20. Measured spectral data of microphones 27, 28 and 29.

data (steady level flight over microphones 1 thru 21) and required emission direction.

Table 2. Computed emission angle compared with closest available measured source location.

Mic #	Computed emission angles	Closest data points
27	(248.1, -5.78)	(249, -11)
28	(254.4, -6.1)	(255, -12)
29	(251.1, -5.74)	(252, -11)

Since microphone 27 is close to the shadow boundary, the scaling factor is ≈ 1 for all frequencies. Figure 21 shows the comparison of the propagated data versus measured spectra. The computed data are close to measured values, with some over predictions at the first tail rotor harmonic (70 Hz), and at higher frequencies around 225 Hz.

There is an error in the near field data used for computation since no data are available at the required emission angles, so the closest measured data points are used. Further, since the source data were measured many seconds further into the run, it is possible that the tail rotor forces have changed for this nominally steady flight, affecting the emitted noise signal. Future work will look into subsequent steady level flight runs to identify if this natural unsteadiness is affecting the results.

Contrary to microphone 27, microphones 28 and 29 are in the shadow region of the hill, where the scaling factor is not 1. For these cases, Equation 10 is used. The frequency spectrum for microphones 29 and 28 is plotted in Figures 22 and 23, respectively, against measured data. Both figures show the computed data with and without scaling. The scaling law impacts frequencies above 5 Hz, with higher frequencies incurring lower attenuation factors, resulting in lower sound intensity.

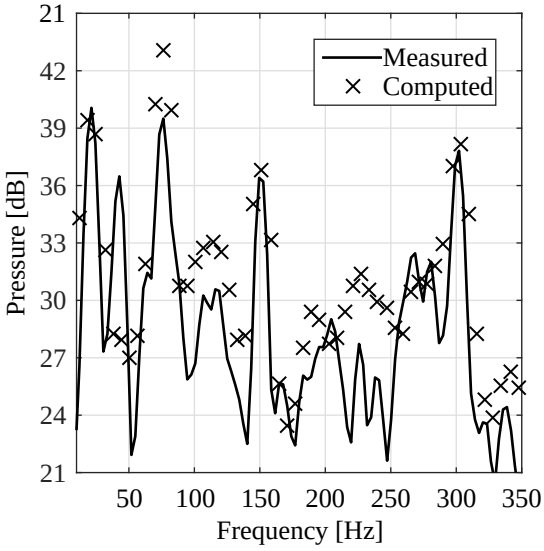

Fig. 21. Microphone 27 spectra, measured data compared wit

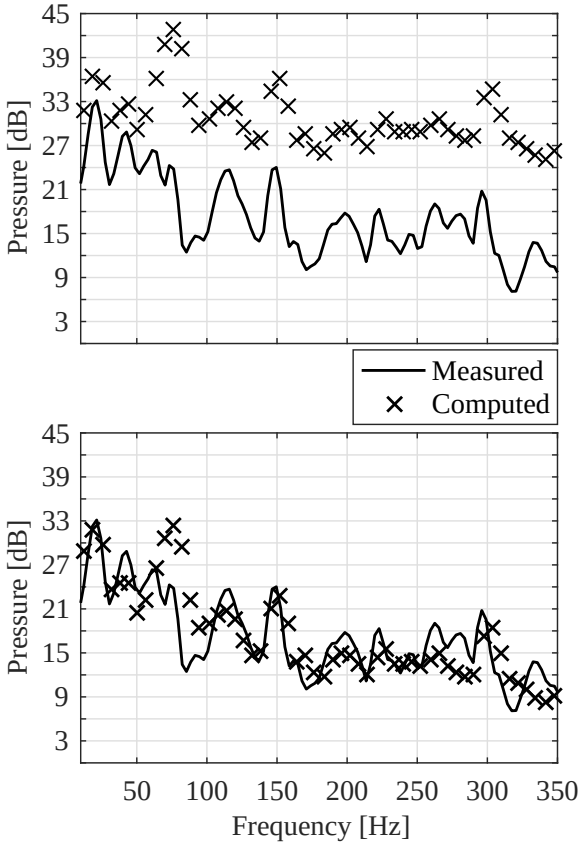

Fig. 22. Measured versus propagated (computed) data for microphone 29. The upper plot includes the computed data without scaling factor applied and the lower plot contains the computed data with the scaling factor applied.

Spectral data from the scaled computation are in good agreement with measured data, although there is a slight overprediction at the first tail rotor harmonic. This overprediction at the tail rotor harmonic is attributed to the lack of adequate

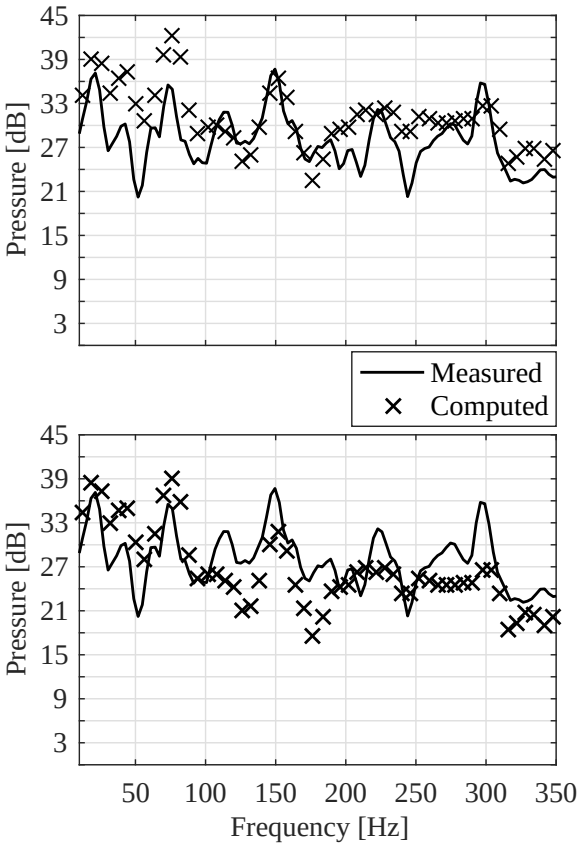

Fig. 23. Measured versus propagated (computed) data for Microphone 28. Top is computed data without scaling factor applied, while bottom has the scaling factor applied.

source noise data for this condition. There are more deviations from measured data for microphone 28 as shown in Figure 23, which will be studied in the future.

Computational errors also exist at microphones 28 and 29, because of the low frequency assumption of the computational wave. As explained before, if there are not enough grid points between two wave passes, the signals can merge due to discretization effects, losing the ability to capture the details of each pass separately and compute interference. If multiple reflections are present in the signal, the implemented computational setup is not currently able to identify them.

CONCLUSIONS

The wave equation (in PDE form) accounts for all the propagation effects such as refraction, multiple reflections, and diffraction. When discretized and numerically evaluated, the propagating waves incur numerical dissipation, which plays a detrimental role in propagation problems. Artificial dissipation is especially problematic when the range is on the order of thousands of wavelengths. For this reason, finite difference methods are replaced by high frequency approximations, which solve an ODE along each ray rather than a collection of rays (or a wave front). Although this is a reasonable approximation for many wave propagation problems, ray tracing tends to fail when diffraction effects are dominant.

Wave Confinement provides a method for solving the wave equation for cases where ray tracing techniques fail. Wave Confinement is a discretization technique that solves the linear wave equation, where the solutions (nonlinear solitary waves) are asymptotically stable. This makes WC a viable choice for long range propagation problems. The asymptotic solutions are representations of physical waves and can be used to propagate details of short waveforms through Dynamic Surface Extension. Since diffraction depends on the frequency, each frequency component of the waveform needs to be resolved separately, which is computationally expensive. To avoid that problem, a physics based scaling law is used to transform information from the computational wavelength to all the physical frequencies within the waveform.

Since the wave length of the nonlinear solitary wave is approximately 5 Hz (for the flight test computations shown in this paper), the scaling factor is 1 at 5 Hz and is < 1 for frequencies greater than 5 Hz. The scaling law plays an important role in capturing the frequency dependent diffraction phenomena, without which Wave Confinement would artificially propagate higher frequency wave fronts into the shadow region. The scaling law that was developed in this paper correctly shielded higher frequency sounds and resulted in quality comparisons with classic diffraction problems as well as flight test acoustics data.

Comparison of Wave Confinement with analytical solutions shows that this new idea is capable of accounting for diffraction effects with reasonable accuracy. A flight test comparison is also completed, with a low frequency assumption that assumes the effects of phase differences between multiple reflected waves are negligible. For example, two wave passes with small phase difference are treated as one pass. Future work will show the capability to compute each pass separately to avoid merging. The flight test comparison showed reasonable agreement with measured data. Further, the propagation method was able to help explain the seemingly anomalous readings from a microphone that was placed in a Poisson spot of an isolated hill.

ACKNOWLEDGMENTS

We acknowledge the U.S. Army SBIR program and AATD for funding this work under contract #W911W6-12C-0036. We also acknowledge Dr. Frank Caradonna for his valuable suggestions and insights, Dr. Arje Nachman for funding under AFOSR contracts and Dr. Eric Greenwood for his insight and assistance on this project.

REFERENCES

[1]Mace, B. L., Bell, P. A., and Loomis, R. J., "Visibility and Natural Quiet in National Parks and Wilderness Areas: Psychological Considerations," *Environment and Behavior*, Vol. 36, (1), January 2004, pp. 5–31.

[2]Lin II, R.-G., "L.A. County backs federal restriction of low-flying helicopters," *LA Times*, Nov 2011.

[3]Vail, E., "Adopt Local Law- Amending Chapter 75 (Airport) of the Town Code Regulating Nighttime Operation of Aircraft at East Hampton Airport," East Hampton Town Board Resolution 2015-411, 2015.

[4]Lighthill, M. J., "On Sound Generated Aerodynamically, I: General Theory," *Proceedings of the Royal Society*, Vol. A221, 1952, pp. 564–587.

[5]Ffowcs Williams, J. E. and Hawkings, D. L., "Sound generated by turbulence and surfaces in arbitrary motion," *Philosophical Transactions of the Royal Society*, Vol. A264, 1969, pp. 321–342.

[6]Farassat, F. and Meyers, M. K., "Extension of Kirchhoffs Formula to Radiation from Moving Surfaces," *Journal of Sound and Vibration*, Vol. 3, (123), 1988, pp. 451–460.

[7]Farassat, F. and Succi, G. P., "A review of propeller discrete frequency noise prediction technology with emphasis on two current methods for time domain calculations," *Journal of Sound and Vibration*, Vol. 71, (3), 1980, pp. 399–419.

[8]Jones, R. M., Riley, J. P., and Georges, T. M., "HARPA: A versatile three-dimensional ray-tracing program for acoustic waves in the atmosphere above irregular terrain," *U.S. Department of Commerce National Oceanic and Atmospheric Administration Environmental Research Laboratories, Wave Propagation Laboratory*, August 1986, pp. 11–12.

[9]Levy, M., "Parabolic Equation Modeling of Propagation over Irregular Terrain," *Radio Science*, Vol. 2, 1990, pp. 1153–1155.

[10]Keller, J., "Geometrical Theory of Diffraction," *Journal of the Optical Society of America*, Vol. 52, 1962, pp. 116–130.

[11]Conner, D. and Page, J., "A Tool for Low Noise Procedures Design and Community Noise Impact Assessment: The Rotorcraft Noise Model (RNM)," *AIAA*, 2002.

[12]Ostashev, V. E., Wilson, D. K., Liu, L., Aldridge, D. F., Symons, N. P., and Marlin, D., "Equations for finite-difference, time-domain simulation of sound propagation in moving inhomogeneous media and numerical implementation," *The Journal of the Acoustical Society of America*, Vol. 117, (2), 2005, pp. 503–517.

[13]Whitham, G., *Linear and nonlinear waves*, John Wiley & Sons, 1974.

[14]Chitta, S., Steinhoff, J., Wilson, A., Caradonna, F., Sim, B., and Sankar, L., "A New Finite-Difference Method for General Long-Range Rotorcraft Acoustics: Initial Comparisons with Intermediate-Range Data," *American Helicopter Society 70th Annual Forum*, 2014.

[15]Steinhoff, J. and Chitta, S., "Solution of the Scalar Wave Equation over Very Long Distances Using Nonlinear Solitary Waves: Relation to Finite Difference Methods," *J. Comput. Phys.*, Vol. 231, (19), 2012, pp. 6306–6322.

[16]Steinhoff, J., Fan, M., and Wang, L., "A New Eulerian Method for the Computation of Propagating Short Acoustic and Electromagnetic Pulses," *Journal of Computational Physics*, Vol. 157, 2000, pp. 683–706.

[17]Osher, S. and Fedkiw, R. P., "Level Set Methods: An overview and some recent results," *Journal of Computational Physics*, Vol. 169, 2001, pp. 463–502.

[18]Born, M. and Wolf, E., *Principles of Optics*, Cambridge University Press, 1959.

[19]Sommerfeld, A., *Optics*, Academic Press, 1954.

[20]Durgin, G., "The Practical Behaviour of Various Edge Diffraction Formulae," *IEEE Antennas and Propagation Magazine*, Vol. 51, (3), June 2009, pp. 24–35.

[21]De Los Santos, H. J., Sturm, C., and Ponte, J., *Radio Systems Engineering: A Tutorial Approach*, Springer Publishing Company, Incorporated, 2014.

[22]Wolfe, P., "Diffraction of a plane wave by a circular disk," *Journal of Mathematical Analysis and Applications*, Vol. 67, (1), 1979, pp. 35–57.

[23]Gu, M., *Advanced Optical Imaging Theory*, Springer Berlin Heidelberg, 2000.

[24]Watts, M. E., Greenwood, E., Sim, B., and Stephenson, J., "Helicopter Acoustic Flight Test with Altitude Variation and Maneuvers," Technical Memorandum NASA/TM-2016-219354, NASA Langley Research Center, Hampton, VA 23681, USA, December 2016.

[25]Greenwood, E. and Schmitz, F. H., "Separation of Main and Tail Rotor Noise Ground–Based Acoustic Measurements Using Time–Domain De-Dopplerization," Proceedings of the 35th European Rotorcraft Forum, Hamburg, Germany, September 2009.